Journal of Energy Storage 28 (2020) 101236

Contents lists available at ScienceDirect

Journal of Energy Storage

journal homepage: www.elsevier.com/locate/est

Natural convection flow of a suspension containing nano-encapsulated phase change particles in an eccentric annulus

S.A.M. Mehryan[a], Mohammad Ghalambaz[b,c,*], Leila Sasani Gargari[d], Ahmad Hajjar[e], Mikhail Sheremet[f]

[a] Young Researchers and Elite Club, Yasooj Branch, Islamic Azad University, Yasooj, Iran
[b] Department for Management of Science and Technology Development, Ton Duc Thang University, Ho Chi Minh City, Vietnam
[c] Faculty of Applied Sciences, Ton Duc Thang University, Ho Chi Minh City, Vietnam
[d] Department of Mechanical Engineering, Shahid Beheshti University, Tehran, Iran
[e] LabECAM, ECAM Lyon, Université de Lyon, Lyon, France
[f] Laboratory on Convective Heat and Mass Transfer, Tomsk State University, Tomsk, Russia

ARTICLE INFO

Keywords:
Nano-encapsulated
Phase change material
Eccentric annulus
Energy storage
Heat transfer control
Free convection

ABSTRACT

The free convective flow of a Nano-Encapsulated Phase Change Material (NEPCM) suspension in an eccentric annulus is investigated numerically. The inner cylinder is heated and kept at a temperature higher than that of the outer cylinder. The core of the NEPCM particles is made of nonadecane while the shell is made of Polyurethane. The nanoparticles are dispersed in water as the base fluid. The equations governing the flow and heat transfer of the NEPCM suspension in the annulus are developed and written in the non-dimensional form. The numerical solutions of these equations are obtained using the finite element method. The validity of the numerical method is ensured by comparing its predictions to the results of previously published studies. The main outcomes point out to the impact of the volume fraction of the NEPCM particles and Stefan number on the thermal and hydrodynamic characteristics of the suspension. A 5% volume fraction represents the optimal value for heat transfer enhancement. Heat transfer is also enhanced when the fusion temperature of the NEPCM core is far from the temperatures of the hot and cold walls. Furthermore, increasing the annulus eccentricity and moving the inner cylinder towards the top tends to inhibit heat transfer in the annulus.

1. Introduction

The rapid growth of energy consumption during the last decades is due to a rise in population, economy, and industry [1,2]. Such high energy utilization level demands to introduce new technical schemes that allow reducing energy consumption. For this purpose, the usage of phase change material to create effective latent thermal energy storage systems [3–5] can be considered as a step to solve the mentioned problem.

Nowadays, there are several published papers on the usage of Phase Change Materials (PCMs) for latent thermal energy systems. Thus, Fadl and Eames [6] have investigated experimentally an opportunity to use the latent heat thermal energy storage system for domestic hot water applications on the basis of the phase change material (paraffin wax RT44HC). They have evaluated a ratio for charging/discharging time. Wang et al. [7] numerically and experimentally have studied the charging-discharging behavior of hydrated salt for latent thermal energy storage. It has been revealed that the optimized fins geometry can essentially diminish the charging and discharging times by at about 25%. Such an approach allows intensifying the heat transfer in PCM systems. Vigneswaran et al. [8] have examined experimentally the heat transfer enhancement in the distillate for the solar stills using PCM. Authors have demonstrated an opportunity to enhance the distillate water production during non-sunshine hours using multiple PCMs in comparison with the conventional solar still and single PCM.

Buonomo et al. [9] have examined computationally the impact of aluminum foam on latent thermal energy storage systems filled with PCM. Analysis has been performed using the local thermal equilibrium approach with the Darcy-Forchheimer model for transport processes in the porous material. They have ascertained that an introduction of metal foam in a system allows improving the energy transport in the considered latent thermal energy storage systems with a rapid melting in comparison with clear PCM. Another work on the heat transfer enhancement in latent heat thermal energy storage using metal foam-PCM

* Corresponding author.
E-mail addresses: mohammad.ghalambaz@tdtu.edu.vn (M. Ghalambaz), ahmad.hajjar@ecam.fr (A. Hajjar), sheremet@math.tsu.ru (M. Sheremet).

https://doi.org/10.1016/j.est.2020.101236
Received 19 October 2019; Received in revised form 27 December 2019; Accepted 22 January 2020
Available online 01 February 2020
2352-152X/

Nomenclature

Latin letters

C_p	the specific heat ($J/kg.\ K$)
Cr	the ratio of the heat capacity of the suspension to the host fluid
f	the non-dimensional form of phase change profile
g	the gravity constant (m/s^2)
H	the characteristic length (m)
h_{sf}	the latent heat of the nanoparticle's core (J/kg)
k	the coefficient of the thermal conductivity ($W/m\ K$)
Nc	the conductivity number for the suspension
Nu	Nusselt number
Nv	the dynamic viscosity number for the suspension
p	the suspension pressure field (Pa)
P	non-dimensional the suspension pressure field
Pr	Prandtl number
Ra	Rayleigh number
Ste	Stefan number
T	the temperature ($^{\circ}C$)
T_{Mr}	the melting temperature range ($^{\circ}C$)
u	the fluid velocity along x axis (m/s)
U	dimensionless fluid velocity along X axis
v	fluid velocity along y axis (m/s)
V	the dimensionless fluid velocity along Y axis
x	x-Cartesian coordinate (m)
X	dimensionless X-Cartesian
y	y-Cartesian coordinate (m)
Y	dimensionless Y-Cartesian coordinate
ι	the weight ratio of the NEPCM particle's core to shell

Greek symbols

μ	the dynamic viscosity of the fluid ($kg\ s/m$)
α	the thermal diffusivity (m^2/s)
β	the coefficient of the volumetric thermal expansion ($1/K$)
δ	the dimensionless phase change band
θ	the non-dimensional temperature field
λ	the dimensionless ratio of the heat capacity
ρ	density (kg/m^3)
ϕ	the volume fraction of particles in the host fluid
Ψ	the stream function

Subscript

a	average
b	the NEPCM suspension
c	the cold wall
co	the core of encapsulated particles
f	the host fluid
fu	the fusion property
h	the hot wall
l	local
p	the NEPCM nanoparticles
sh	the shell of NEPCM particle

composite has been performed by Joshi and Rathod [10]. They have studied the metal foam properties for a reduction of the charging time for PCM. As a result, it has been revealed that the metal foam can diminish the weight of the latent heat thermal energy storage system.

Experimental analysis of paraffin wax RT35 behavior in a shell and helical tube heat exchanger has been performed by Rahimi et al. [11]. They have considered a double pipe heat exchanger containing a helical tube in order to intensify the charging process of PCM. A theoretical investigation based on exergy analysis has been conducted, and the authors determined that the usage of a helical tube allows intensifying the melting process and decreasing the charging time for PCM. Numerical simulation of heat transfer performance of a silicon-based latent heat thermal energy storage system has been conducted by Zeneli et al. [12]. They have used ANSYS Fluent software for computational study with the enthalpy-porosity technique. During the calculations different shapes of the PCM container have been examined. The obtained results have shown that during the melting process with heating from sidewalls, the heated surface has an essential influence on the PCM melting intensity. As a result, the cubic shape having biggest heated surface is characterized by the highest melting intensity.

An inclusion of nanoparticles to PCM can enhance the thermal conductivity of substance and improve the energy transport characteristics. Thus, comprehensive review on nano-enhanced PCM has been prepared by Leong et al. [13]. Authors have shown the possibility to enhance the energy transport in PCM using nanoparticles and the applications of such nano-enhanced PCM have been studied. Gorzin et al. [14] have addressed the effect of utilizing Cu nanoparticles-additives on the solidification of PCMs in a shell and multi-PCM-tube heat exchanger. They reported that the optimal mass of nanoparticles is needed to realize a uniform temperature distribution inside the shell's working fluid. Abdulateef et al. [15] have considered computationally and experimentally thermal behavior and liquid circulation within the triplex-tube heat exchanger under the influence of alumina nanoparticles and paraffin. It has been illustrated that the usage of nanoparticles and fins can enhance the PCM discharging (solidification). In the case of cooling of heat-generating elements, Bondareva et al. [16] have shown that an addition of alumina nanoparticles to n-octadecane can change the charging time in dependence on the heat sink orientation. More essential reduction of the charging time can be found when the heat-generating element and the heat sink are located on the upper part of the cavity.

It is worth noting that PCM can be included in micro or nano capsules that allow augmenting the energy transport. Thus, Rodriguez-Cumplido et al. [17] discussed an opportunity to use micro-encapsulated PCMs and nano-encapsulated PCMs in order to store or transport the thermal energy. They showed advantages to employ an additional shell for PCM that can raise the thermal conductivity, produce magnetic NEPCM or to improve the mechanical properties of NEPCM. Interesting and useful results for the nano-encapsulated PCM have been obtained by Ghalambaz et al. [18] and Hajjar et al. [19]. It has been found that the presence of nano-encapsulated PCM particles augments the energy transport within the region.

The geometry of eccentric tubes have various applications in PCM heat storage units [20–23] and tube solar collector [24]. Due to the natural convection and the solar radiation effects, the eccentricity of the inner tube is an essential aspect of the design of shell and tube thermal energy storage enclosures and solar collectors.

The literature review shows that the phase change materials are extensively employed as a thermal energy storage medium. However, the poor conduction heat transfer of PCMs has been the primary barrier to the practical applications of PCMs. Suspending nano-encapsulated particles in a host liquid is a novel and practical approach for promising improving the heat transfer process during the thermal energy storage/release of PCMs. However, there are only few studies regarding the thermal energy storage and energy transport of nano-encapsulated materials in passive systems [18,19], operation based on the natural convection mechanisms. The present study aims to model the natural convection thermal behavior of a suspension of NEPCMs in a shell and tube (2D annulus) thermal energy storage medium. The analysis of the thermal behavior of phase-change nanoparticles is essential for future

design and application of NEPCM nanofluids and slurries.

2. Physical model

A two-dimensional annulus filled with a suspension of water and nano-encapsulated phase change particles is considered, and the schematic view of the model is illustrated in Fig. 1. The annulus is assumed long, and hence, it is modeled as a 2D domain. The water contains nano-encapsulated phase change particles with a volume fraction ϕ, and the suspension filled the space between the hot inner cylinder and cold outer cylinder. The inner and outer cylinders are shown as circles in the 2D domain. The NEPCM particles, as depicted in an exaggerating magnetified size in Fig. 1, are made of a PCM core and a shell. The PCM core of the nanoparticles can undergo a liquid/solid phase change and absorb/release latent heat at a fusion temperature of T_{fu}. A cycle of phase change for a nano-encapsulated phase change particle is depicted in Fig. 1 in the states of A (solid cold-corenormal), B (normal), and C (liquid hot-core). These NEPCM particles are suspended in the water.

The eccentricity, i.e. e, is the distance between the centers of the outer and inner cylinders. Also, γ is an angle between the x-axis and the line connecting the centers of the cylinders. As indicated in Fig. 1, the inner cylinder, located at (x_i, y_i), is heated at the temperature of T_h above the temperature of T_c of the outer cylinder. The heating of the inner cylinder can be due to a flow of a hot liquid in the inner cylinder, evaporation of a liquid, or an electrical element. The cooling of the outer cylinder can be due to a strong convection with cold fluid, or a condensation of a vapor over the wall of the external cylinder. The space outside of the cold cylinder and space inside of the hot cylinder is not a part of the physical model and domain of the solution, and they only act as the boundary condition for the model.

The radii ratio, i.e. r_o/r_i, is R_r. The shell is made of a polymer, polyurethane (PU), while the core is made of a phase change material, Nonadecane. The NEPCM suspension is uniform, and there is no significant slip mechanism between the nanoparticles and the host fluid. As the encapsulated particles are tiny, there is no notable temperature gradient in the particles, and hence, the lamped model for nanoparticles and phase change in the core of particles is applicable. The essential properties of the core, host fluid, and the shell are summarized in Table 1. In addition, the core fusion-temperature of NEPCM is around 32 °C while the latent heat of the core is 211 kJ/kg [25].

2.1. The mathematical formulation

Considering the modeling assumptions, the equations governing equations for modeling hydro-dynamic and thermal and behavior of an incompressible and laminar suspension are as follows:

Table 1
Thermophysical properties of NEPCM-core, NEPCM-shell and the host fluid [25].

	k (W/m.K)	C_p (KJ/kg.K)	ρ (kg/m^3)	μ (kg/m. s)	β (K^{-1})
Nonadecane	—	2037	721	—	—
Host fluid	0.613	4179	997.1	8.9×10^{-4}	21×10^{-5}
PU	—	1317.7	786	—	17.28×10^{-5}

The conservation of mass (continuity):

$$\left(\frac{\partial u}{\partial x} + \frac{\partial v}{\partial y}\right) = 0 \tag{1}$$

The conservation of momentum

$$\rho_b u\frac{\partial u}{\partial x} + \rho_b v\frac{\partial u}{\partial y} = -\frac{\partial p}{\partial x} + \mu_b\left(\frac{\partial^2 u}{\partial x^2} + \frac{\partial^2 u}{\partial y^2}\right) \tag{2-a}$$

$$\rho_b u\frac{\partial v}{\partial x} + \rho_b v\frac{\partial v}{\partial y} = -\frac{\partial p}{\partial y} + \mu_b\left(\frac{\partial^2 v}{\partial x^2} + \frac{\partial^2 v}{\partial y^2}\right) + g\rho_b\beta_b(T - T_c) \tag{2-b}$$

The conservation of energy

$$(\rho C_p)_b u\frac{\partial T}{\partial x} + (\rho C_p)_b v\frac{\partial T}{\partial y} = k_b\left(\frac{\partial^2 T}{\partial x^2} + \frac{\partial^2 T}{\partial y^2}\right) \tag{3}$$

In the above equations, u and v are the velocity components in x and y directions, ρ is density, μ is dynamic viscosity, β is the thermal expansion coefficient, g is the gravity, T is the temperature, C_p is the specific heat capacity, k is the thermal conductivity. The subscript of b of the above-written equations indicates the bulk properties of the NEPCM suspension. According to the problem physics, the boundary conditions are

$$\forall\, x, y | (x - x_i)^2 + (y - y_i)^2 = r_i^2 \Rightarrow u = v = 0,\ T = T_h \tag{4-a}$$

$$\forall\, x, y | x^2 + y^2 = r_o^2 \Rightarrow u = v = 0,\ T = T_c \tag{4-b}$$

In which, x_i, y_i and r_i are the center characteristic and radius of the inner cylinder, and r_o is the radius of the outer one.

2.2. Bulk properties of the suspension

The density of the NEPCM-suspension is evaluated as a weighted function of the NEPCM dispersed-particles and host fluid as [26]

$$\rho_b = (1 - \phi)\rho_f + \phi\rho_p \tag{5}$$

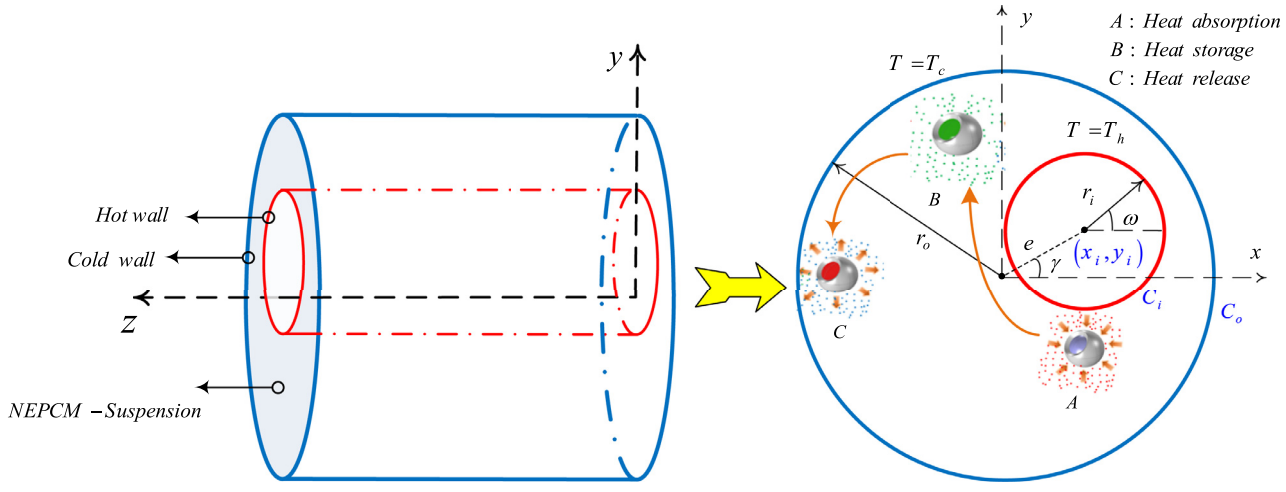

Fig. 1. Configuration view of the problem physics.

The p and f subscripts denote NEPCM particles and the base fluid, respectively. ϕ is the concentration of the NEPCMs particles. The density of NEPCM particles is evaluated as follows [26]

$$\rho_p = (1+\iota)(\rho_{co}\rho_{sh})(\rho_{sh}+\iota\rho_{co})^{-1} \tag{6}$$

ρ_{sh} and ρ_{co} are respectively the densities of the shell and core of NEPCM particles. ι is the core-shell weight ratio and is about $\iota \sim 0.447$ [25]. In addition, the density of the core is an average of the solid and liquid phases of the phase change substance. The specific heat capacity of the suspension is calculated as [27,28]

$$C_{p,b} = \rho_b^{-1}(\rho_f C_{p,f}(1-\phi) + \rho_p C_{p,p}\phi) \tag{7}$$

The effective heat capacity of an encapsulated phase change nanoparticles, $C_{p,\,p}$, can be computed by the following equation [26]

$$C_{p,p} = \rho_p^{-1}(C_{p,co} + \iota C_{p,sh})(\rho_{co}\rho_{sh})(\rho_{sh}+\iota\rho_{co})^{-1} \tag{8}$$

It is worth mentioning that the specific heat capacity of the core of encapsulated nanoparticles is the average of the heat capacities of the fluid and solid phases. Since the core of the nanoparticles experiences a phase change, the latent heat of change-phase is involved in the specific heat capacity of the nanoparticles. The latent heat can be modeled by employing rectangular, triangle or sinusoidal profiles as follows [26,29]:

$$C_{p,p} = C_{p,co} + \frac{h_{sf}(T - T_{fu} + T_{Mr}/2)}{T_{Mr}} \tag{9-a}$$

$$C_{p,p} = C_{p,co} + \left\{\frac{\pi}{2}\cdot\left(\frac{h_{sf}}{T_{Mr}} - C_{p,co}\right)\cdot\sin\left(\pi\frac{T - T_{fu} + T_{Mr}/2}{T_{Mr}}\right)\right\} \tag{9-b}$$

$$C_{p,p} = C_{p,co} + 2\left(\frac{h_{fs}}{T_{Mr}^2} - \frac{C_{p,co}}{T_{Mr}}\right)(T - T_{fu} + T_{Mr}/2) \tag{9-c}$$

T_{Mr} is the temperature interval. In fact, this interval avoids the discontinuity in energy balance. The total specific heat capacity of the nanoparticle's core, comprising the sensible and latent heats are defined based on T_{Mr} [26,29]

$$C_{p,p} = C_{p,co} + \left\{\frac{\pi}{2}\cdot\left(\frac{h_{sf}}{T_{Mr}} - C_{p,co}\right)\cdot\sin\left(\pi\frac{T - T_{fu} + T_{Mr}/2}{T_{Mr}}\right)\right\}\gamma$$
$$\gamma = \begin{cases} 0 & T < T_{fu} - T_{Mr}/2 \\ 1 & T_{fu} - T_{Mr}/2 < T < T_{fu} + T_{Mr}/2 \\ 0 & T > T_{fu} + T_{Mr}/2 \end{cases} \tag{10}$$

The coefficient of thermal volume-expansion for the NEPCM-suspension is written as [29]

$$\beta_b = (1-\phi)\beta_f + \phi\beta_p \tag{11}$$

The effective thermal conductivity and dynamic viscosity of the NEPCM-suspension are evaluated using linear relations presented below [30,31]

$$\frac{k_b}{k_f} = 1 + Nc\phi \tag{12-a}$$

$$\frac{\mu_b}{\mu_f} = 1 + Nv\phi \tag{12-b}$$

Nc and *Nv* of the above relations respectively denote the numbers of thermal conductivity and dynamic viscosity. As discussed in [30,31], the coefficients of *Nc* and *Nv* are a function of various parameters such as type and size of nanoparticles, the type of the host fluid, temperature, synthesis method of nanofluid preparation. However, these values can be considered fixed for a synthesized nanofluid. It should be noted that Eq. 12 is sufficient for low volume fractions of nanoparticles, $\phi \le 0.5\%$.

2.3. Non-dimensional form of governing equations

A non-dimensional form of the governing equation can exhibit a general behavior of the NEPCM suspension. Hence, the following non-dimensional variables are invoked to transform the governing equations and their boundary conditions into a general non-dimensional form

$$X = \frac{x}{H},\ Y = \frac{y}{H},\ R_i = \frac{r_i}{H},\ R_o = \frac{r_o}{H},\ E_c = \frac{e}{H},\ U = \frac{uH}{\alpha_f}$$
$$V = \frac{vH}{\alpha_f},\ P = \frac{pH^2}{\rho_f\alpha_f^2},\ \theta = \frac{T - T_c}{\Delta T} \tag{13}$$

where $H = r_o - r_i$ and $\Delta T = T_h - T_c$. Invoking the non-dimensional parameters, we then have:

$$\frac{\partial U}{\partial X} + \frac{\partial V}{\partial Y} = 0 \tag{14}$$

$$\left(\frac{\rho_b}{\rho_f}\right)\left(U\frac{\partial U}{\partial X} + V\frac{\partial U}{\partial Y}\right) = -\frac{\partial P}{\partial X} + Pr\left(\frac{\mu_b}{\mu_f}\right)\left(\frac{\partial^2 U}{\partial X^2} + \frac{\partial^2 U}{\partial Y^2}\right) \tag{15}$$

$$\left(\frac{\rho_b}{\rho_f}\right)\left(U\frac{\partial V}{\partial X} + V\frac{\partial V}{\partial Y}\right) = -\frac{\partial P}{\partial Y} + Pr\left(\frac{\mu_b}{\mu_f}\right)\left(\frac{\partial^2 V}{\partial X^2} + \frac{\partial^2 V}{\partial Y^2}\right)$$
$$+ Ra\cdot Pr\left(\frac{\rho_b}{\rho_f}\right)\left(\frac{\beta_b}{\beta_f}\right)\theta \tag{16}$$

The non-dimensional parameters appeared in the above-written equations, Rayleigh *Ra* and Prandtl *Pr* numbers, are:

$$Ra = \frac{g\rho_f\beta_f\Delta T H^3}{\alpha_f\mu_f},\ Pr = \frac{\mu_f}{\rho_f\alpha_f} \tag{17}$$

Also,

$$\left(\frac{\beta_b}{\beta_f}\right) = (1-\phi) + \phi\frac{\beta_p}{\beta_f},\ \left(\frac{\rho_b}{\rho_f}\right) = (1-\phi) + \phi\frac{\rho_p}{\rho_f} \tag{18}$$

In the present study, it is assumed that NEPCM particles expand the same as the water (host fluid), and as there is no slip mechanism between the base fluid and NEPCMs, the thermal expansion ratio is approximated as $\beta_b/\beta_f \sim 1$.

$$Cr\left(U\frac{\partial\theta}{\partial X} + V\frac{\partial\theta}{\partial Y}\right) = \left(\frac{k_b}{k_f}\right)\left(\frac{\partial^2\theta}{\partial X^2} + \frac{\partial^2\theta}{\partial Y^2}\right) \tag{19}$$

where

$$Cr = \frac{(\rho C_p)_b}{(\rho C_p)_f} = (1-\phi) + \phi\lambda + \phi\delta^{-1}Ste^{-1}f \tag{20}$$

Herein, *Cr* is the ratio of heat capacity of the suspension to the sensible heat capacity of the host fluid. Furthermore, the sensible heat capacity ratio (λ), the non-dimensional melting interval (δ) and Stefan number (*Ste*) are introduced as

$$\lambda = \frac{(C_{p,co} + \iota C_{p,sh})\rho_{co}\rho_{sh}}{(\rho C_p)_f(\rho_{sh} + \iota\rho_{co})},\quad \delta = \frac{T_{Mr}}{\Delta T},\quad Ste = \frac{(\rho C_p)_f\Delta T(\rho_{sh} + \iota\rho_{co})}{\alpha_f(h_{sf}\rho_{co}\rho_{sh})} \tag{21}$$

In addition, f, the non-dimensional fusion function, is introduced as:

$$f = \frac{\pi}{2}\sin\left(\frac{\pi}{\delta}(\theta - \theta_{fu} + \delta/2)\right)\sigma$$
$$\sigma = \begin{cases} 0 & \theta < \theta_{fu} - \delta/2 \\ 1 & \theta_{fu} - \frac{\delta}{2} < \theta < \theta_{fu} + \delta/2 \\ 0 & \theta > \theta_{fu} + \delta/2 \end{cases} \tag{22}$$

Here, θ_f, the non-dimensional fusion temperature, is:

$$\theta_{fu} = \frac{T_{fu} - T_c}{\Delta T} \tag{23}$$

Eventually, the non-dimensional form of boundary conditions can be obtained as:

$$\forall X, Y | (X - X_i)^2 + (Y - Y_i)^2 = R_i^2 \Rightarrow U = V = 0, \theta = 1 \quad (24\text{-a})$$

$$\forall X, Y | X^2 + Y^2 = R_o^2 \Rightarrow U = V = 0, \theta = 0 \quad (24\text{-b})$$

where (X_i, Y_i) presents the location of the inner cylinder. The local heat transfer through the hot wall is obtained using the relation given below:

$$Nu_l = -(1 + Nc\phi)\left(\frac{\partial \theta}{\partial n}\right)_{C_i} \quad (25)$$

The integration of the above equations gives the total heat transfer rate:

$$Nu_a = \frac{1}{2\pi}\int_0^{2\pi} Nu_l d\omega \quad (26)$$

The effect of dispersing the nano-encapsulated particles can be investigated by introducing the following normalized average Nusselt numbers:

$$Nu_r = \frac{Nu_a|_\phi}{Nu_a|_{\phi=0}}, Nu_r' = \frac{Nu_a|_{\phi, Ste\to\infty}}{Nu_a|_{\phi=0}}, Nu_r'' = \frac{Nu'_{rr}}{Nu_r} = \frac{Nu_a|_{\phi, Ste\to\infty}}{Nu_a|_\phi} \quad (27)$$

$Nu_a|_{\phi=0}$ is the time-averaged Nusselt number associated with the host fluid. Nu_r evaluates the impact of the presence of the NEPCM particles on the heat transfer rate compared with the host fluid. Nu_r' represents the increasing or decreasing effects of NEPCMs particles with no phase change on the heat transfer rate. Furthermore, the influence of phase change of PCM core on the Nu_a is investigated by Nu_r''. In fact, when Stefan number reaches infinity, the latent heat tends to zero, and the phase change does not play any role in the heat transfer.

Also, streamlines which can be a good way to visualize the suspension flow is achieved by solving the following Poisson equation:

$$\left(\frac{\partial^2 \Psi}{\partial X^2} + \frac{\partial^2 \Psi}{\partial Y^2}\right) = \frac{\partial U}{\partial Y} - \frac{\partial V}{\partial X} \quad (28)$$

where the walls are considered as streamlines with zero magnitudes.

3. Numerical approach and mesh test

The governing equations consisting of continuity, momentum, and energy ones, along with the boundary conditions are solved using the Galerkin finite element method (FEM). The damped Newton scheme is used to couple the dimensionless governing equations for the velocity and temperature fields. The Parallel Sparse Direct Solver is adopted to solve the equivalent linear algebraic equations (see Appendix A). Gaussian quadrature with second-order accuracy is applied to integrate the integral residuals of Eqs. (A2)–(A6). Integration the residual equations for each element leads to an implicit set of algebraic equations (residual equations), including the unknown value of the filed variables. At each element, there are five unknowns, which are *X*-velocity (*U*), *Y*-velocity (*V*), pressure (*P*), temperature (θ), and streamline value (ψ). The set of residual equations for the entire domain construct an extensive set of algebraic equation, which has to be solved numerically for the unknown variables. The Newton method using the PARallel DIrect SOlver (PARDISO), is utilized to solve the residual equations iteratively [32–34]. The PARDISO [35] is a memory-efficient, robust, and high-performance library for solving large sparse linear systems of equations on shared-memory multiprocessors. The error convergence for each of the dependent variables is not more than 10^{-5}.

A non-uniform structural mesh, as demonstrated in Fig. 2, is employed to discretize the computational fluid domain. The mesh-independency for the present work to check the mesh stability is shown in Table 2. The results of the mesh-independency test are average Nusselt number on the hot inner cylinder and absolute maximum stream function for the case of $Ra = 5 \times 10^4$, $E_c = 0.67$, $Ste = 0.2$, $\phi = 0.05$, $\theta_f = 0.05$, $\gamma = -\pi/4$, $Nc = 23.8$, $Nv = 12.5$, $\lambda = 0.322$, and $R_r = 2.5$. The information about this parameter will be introduced in the next section. The number of elements started with 20 × 40 and finished by 95 × 190. The results of Table 2 show that the mesh size of 50 × 100 can provide accurate results up to two decimal points, which is acceptable for most of engineering applications. Increasing the mesh-size (a finer mesh with higher number of computational elements) increases both the accuracy of the results, but it also raises the computational costs. Hence, in order to keep the computational costs fair with adequate accuracy, the mesh-size of 50 × 100 is adopted for the computations of the results of the present study.

The outcomes of the present research are compared with two works published to validate the correctness of the utilized code. At the first stage, the average Nusselt numbers of the current study and those reported by Matin and Pop [36] are compared. Matin and Pop [36] conducted the study of natural convection flow inside an annulus occupied by Cu-water nanofluid. The average Nusselt numbers for the different values of volume fraction of the nanoparticles of the current calculations and those presented by Matin and Pop [36] are tabulated in Table 3. Clearly, a quite satisfactory agreement between the outcomes of Matin and Pop [36] and ours are found.

In the second stage, the outcomes of the current solution are further verified by comparing the heat transfer rates obtained from applied code in this paper with the heat transfer rates presented by Turan et al. [37]. In the work of Turan et al. [37], the study of the natural convection heat transfer inside a cavity was conducted. The high and low temperatures were imposed on the left and right vertical walls, and the other walls were adiabatically isolated. The comparison between the results of the current work and the results given by Turan et al. [37] are depicted in Fig. 3. The results are reported for $Pr = 1000$ and $Ra = 10^5$. As can be seen from Fig. 3, an excellent matching can be observed. As can be seen from Fig. 3, an excellent matching can be observed. The correctness of the results of the present work is further validated by comparing the new results and those presented in [38], as depicted in Fig. 4. Kuehn and Goldstein [38] conducted an experimental study to extend existing knowledge of the flow and heat transfer characteristics inside a horizontal annulus. The high matching between the numerical results of the present work and the experimental results of Kuehn and Goldstein [38] confirms that the utilized code is reliable and accurate so enough.

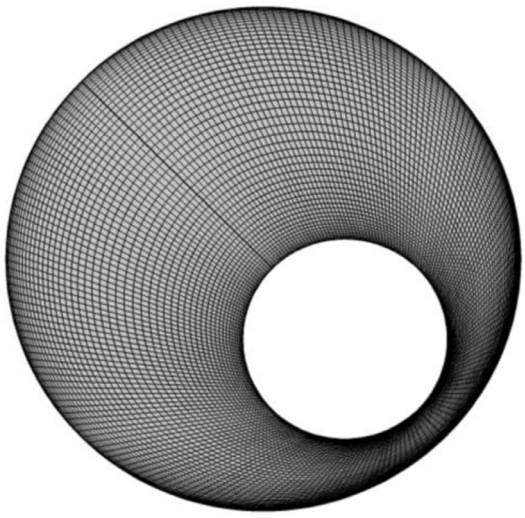

Fig. 2. Utilized grid to discretize the domain.

Table 2
The mesh independency-check results.

Number of elements	20 × 40	35 × 70	**50 × 100**	65 × 130	80 × 160	95 × 190
Nu_a	8.3387	8.3481	**8.3504**	8.3511	8.3515	8.3518
Ψ_{max}	51.120	51.200	**51.219**	51.227	51.231	51.233

Table 3
Average Nusselt number computed in the current works and literature results reported by Matin and Pop [36] for $E_c = 0.5$, $\gamma = \pi/2$, $Pr = 6.21$ and $Ra = 10^5$.

Volume fraction	Matin and Pop [36]	Present work	difference
0.01	5.66	5.60	1.07%
0.02	5.89	5.86	0.51%
0.03	6.02	6.07	0.82%

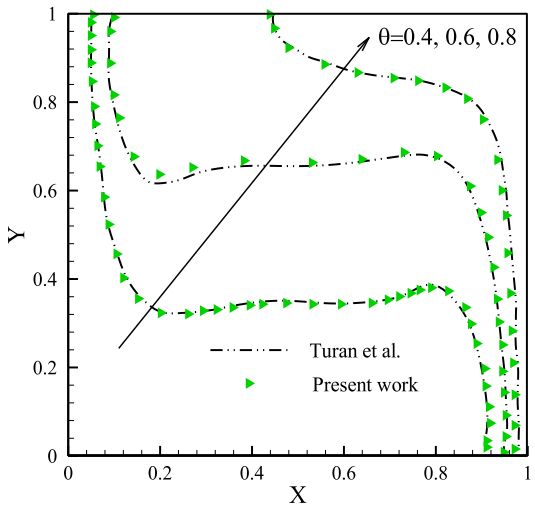

Fig. 3. Temperature distribution obtained in the current code and by Turan et al. [37].

Fig. 4. Comparison between temperature of the present study (left) and experimental one (right) [38] for $Pr = 0.706$, $E_c = 0$, and $Ra = 4.7 \times 10^4$.

4. Results and discussions

In the present study, the flow and heat transfer of NEPCM-suspension in an annulus of the eccentric horizontal cylinders are investigated. The thermal conductivity (Nc) and dynamic viscosity (Nv) numbers are set as $Nc = 23.8$ and $Nv = 12.5$. The values of Nc and Nv are computed using the experimental data reported by Barlak et al. [25]. In addition, the sensible heat capacity ratio (λ) is set to 0.322 based on the same data. Moreover, the radii ratio, i.e. R_r, and Rayleigh number are fixed at 2.5 and 5×10^4, respectively. The numerical simulations are conducted for the following parameters: Stefan number $0.2 \leq Ste \leq \infty$, eccentricity $0.0 \leq E_c \leq 0.75$, eccentricity angle $-\pi/2 \leq \gamma \leq \pi/2$ and the NEPCM volume fraction $0.0 \leq \phi \leq 5\%$. The dimensionless fusion temperature is also adopted in the range of $0.05 \leq \theta_f \leq 0.95$. In order to study the effect of one parameter on the thermal and hydrodynamic behaviors of the suspension in the annulus, its value is varied in the introduced range, while the remaining parameters are kept constant.

Fig. 5 depicts the streamlines, the isothermal contours and the contours of the heat capacity ratio Cr in the annulus for different values of the eccentricity E_c. When the two cylinders are concentric ($E_c = 0$), the streamlines present a symmetry around the inner cylinder. In that case, as the hot fluid moves up, two identical streamline patterns appear on both sides of the inner cylinder starting from the bottom. When the eccentricity is increased to $E_c = 0.4$, the inner cylinder shifts to the right, and the streamline patterns are no more symmetric, as the space of fluid flow is altered. Further increasing the eccentricity to $E_c = 0.75$ leads to a more developed flow on the left of the inner cylinder, while almost no flow is occurring above it. The velocity vectors indicate that the fluid is circulating in the counterclockwise direction in the region at the left of the inner cylinder and in the opposite direction in the region at its right. Indeed, as the inner cylinder is heated, the temperature of the fluid close to it rises and the fluid moves upwards, while the cold fluid moves downwards, mainly near the cold outer cylinder, which explains the circulation direction inside the annulus.

As for the isotherms, in all cases, they start in a circular shape near the cold cylinder in the upper side of the annulus then deviate towards the hot wall. In addition, the isotherms are concentrated above the inner cylinder. In the case of concentric cylinders, the isothermal contours are symmetrical around the inner cylinder. This symmetry vanishes when E_c is increased, and the isothermal contours get more prolonged in the left region of the annulus as the inner cylinder is moved towards the right. However, the location of the isotherms is not greatly affected by the increase of E_c. In the depiction of Cr, the red zone corresponds to the zone where the PCM core of the NEPCM particles undergoes a phase change. As the fusion temperature is set $\theta_f = 0.05$, which is close to the cold wall temperature, the zone of phase change follows the corresponding isotherm and remains close to the outer cold-cylinder. Overall, changing E_c does not seem to substantially affect the location of the PCM phase change in the annulus.

The streamlines and the contours of the isotherms and Cr for different values of the eccentricity are plotted in Fig. 6. The two cylinders are not concentric as the eccentricity is fixed at $E_c = 0.75$. For $\gamma = -\pi/2$, two identical recirculation patterns with different flow directions, as indicated by the velocity vectors, are developed to the right and the left of the inner cylinder as the convective flow is occurring in the annulus. As the inner cylinder is shifted towards the right ($\gamma = -\pi/4$; $\gamma = 0$), the flow becomes more developed to the left of the inner cylinder. When the inner cylinder is moved to the top, similar behavior is observed when comparing the case $\gamma = -\pi/2$ to $\gamma = \pi/2$ and the case $\gamma = -\pi/4$ to $\gamma = \pi/4$, but with less concentrated streamlines in the case of positive γ, as the presence of the inner cylinder near the top slows down the upward motion of the hot fluid.

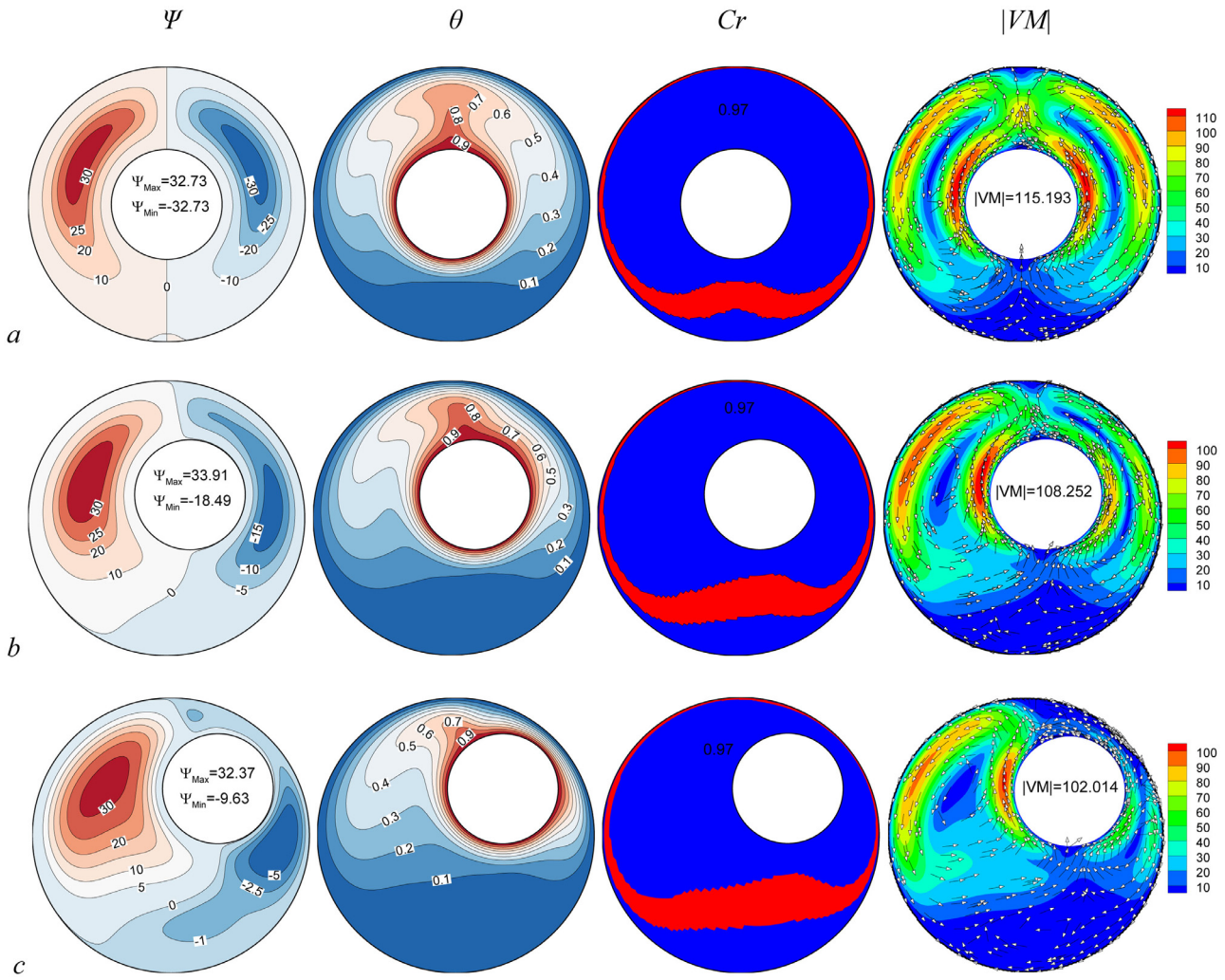

Fig. 5. Dependency of the governing fields on the eccentricity (a: $E_c = 0.0$, b: $E_c = 0.4$, c: $E_c = 0.75$) when $Ra = 5 \times 10^4$, $\phi = 5\%$, $\theta_f = 0.05$, $\gamma = \pi/4$, and $Ste = 0.2$.

The distribution of the isothermal contours is affected by γ. The isotherms start near the cold wall in all the cases and follow the flow development in the annulus. As the emplacement of the inner cylinder is changed, the location of high-temperature gradients varies accordingly. By consequence, the variation of γ affects the contours of *Cr*. The PCM phase change occurs in a zone where the temperature is close to θ_f. Due to the change in the isothermal contours, the pattern of the isotherms corresponding to temperatures close to θ_f changes, and a consequent difference in the *Cr* contours appear.

The effect of the fusion temperature θ_f on the streamlines and the isothermal and *Cr* contours is illustrated in Fig. 7. In all the cases, two recirculation zones are present the convective flow occurring in the cavity. As previously mentioned, it can be seen in the plot of the velocity vectors that the direction of circulation is different in the two zones, due to the heating of the inner cylinder. The size of the zone to the left is greater than the other zone due to the location of the inner cylinder which is shifted towards the right. It is clear that the streamlines present similar patterns when θ_f is varied. However, for higher values of θ_f, the streamlines are concentrated, indicating a more intense flow. Changing θ_f does not greatly affect the isothermal contours. The isotherms are similar near the walls in all the cases, and slight difference can be observed in the elongation of the isotherms in the zone between the cylinders. The clearest effect of varying θ_f is on the contours of *Cr*. For $\theta_f = 0.05$, the phase change occurs in a limited zone near the outer cold-cylinder while it takes place near the inner hot wall for $\theta_f = 0.8$. For $\theta_f = 0.4$, a larger zone of phase change appears in the space between the two cylinders.

Fig. 8 shows the variation of the average Nusselt number Nu_a and the normalized average Nusselt number Nu_r as functions of θ_f for different values of the NEPCM volume fraction ϕ. It is shown that for all the values of θ_f, Nu_a increases with the rise of ϕ and is maximum for $\phi = 0.05$. Indeed, more latent heat is included in the heat transfer when a greater fraction of NEPCM particles is present in the flow. The optimal volume fraction for a dilute NEPCM suspension is 5%. Fig. 8(b) shows that using a suspension of 5% NEPCM volume fraction increases the heat transfer rate by up to 80%. In addition, it is shown that θ_f slightly affects Nu_a where a minimum is obtained for $\theta_f = 0.05$ and $\theta_f = 0.95$, i.e. when the fusion temperature is close to the temperature of the hot wall or to that of the cold one. In fact, as previously mentioned, the PCM undergoes phase change when the temperature surrounding it is close to θ_f. When θ_f is close to one of the cylinder's temperature, the zone of phase change becomes limited (see Fig. 7), and the involvement of the NEPCM particles in heat transfer is diminished. The opposite happens when θ_f is far from the cylinder temperatures.

Fig. 9 depicts the variation of the normalized average Nusselt number Nu_r' as a function of ϕ. It shows that Nu_r' increases with ϕ and reaches its maximum for $\phi = 0.05$. This result confirms the observations discussed in Fig. 8. Heat transfer is enhanced by dispersing NEPCM particles in the flow. Respecting the assumption of dilute suspension, using a 5% volume fraction of NEPCM particles provides the

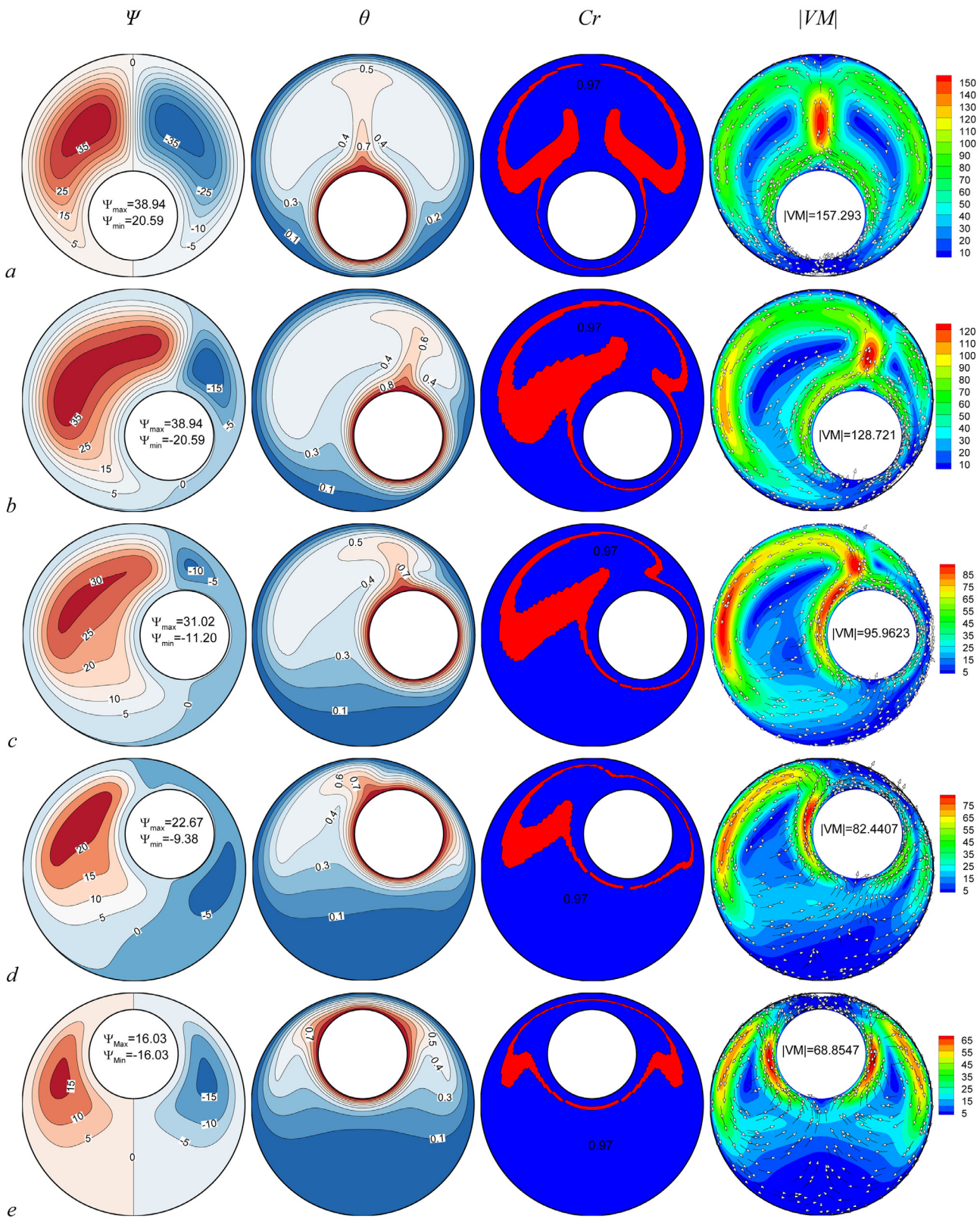

Fig. 6. Dependency of the governing fields on the γ (a: $\gamma = -\pi/2$, b: $\gamma = -\pi/4$, c: $\gamma = 0$, d: $\gamma = \pi/4$, e: $\gamma = \pi/2$) when $Ra = 5 \times 10^4$, $\phi = 5\%$, $\theta_f = 0.4$, $Ste = 0.2$, and $E_c = 0.75$.

best heat transfer in the annulus.

The variation of Nu_a as a function of θ_f for various values of Stefan number Ste is shown in Fig. 10. It is clear that decreasing Ste raises Nu_a for most of the values of θ_f. A decrease in Ste indicates that the latent heat of the PCM core is increased. In that case, the contribution of the NEPCM particles to the overall heat transfer in the annulus is augmented, and heat transfer is enhanced as shown by the increase of Nu_a. However, this rise is not apparent for $\theta_f = 0.05$ and $\theta_f = 0.095$, where

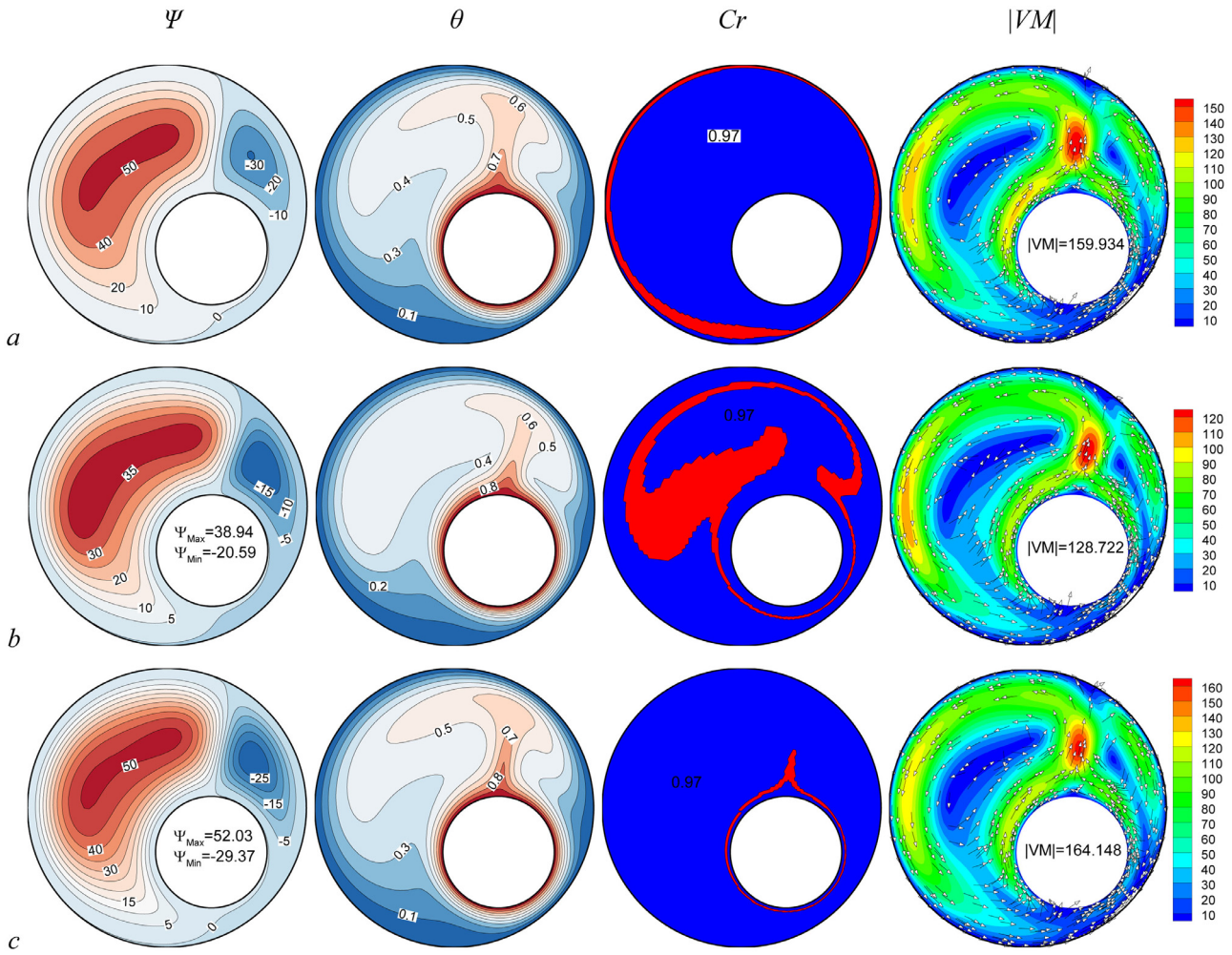

Fig. 7. Dependency of the governing fields on the θ_f (a: $\theta_f = 0.05$, b: $\theta_f = 0.4$, c: $\theta_f = 0.8$) when $Ra = 5 \times 10^4$, $\phi = 5\%$, $\gamma = -\pi/4$, $Ste = 0.2$, and $E_c = 0.75$.

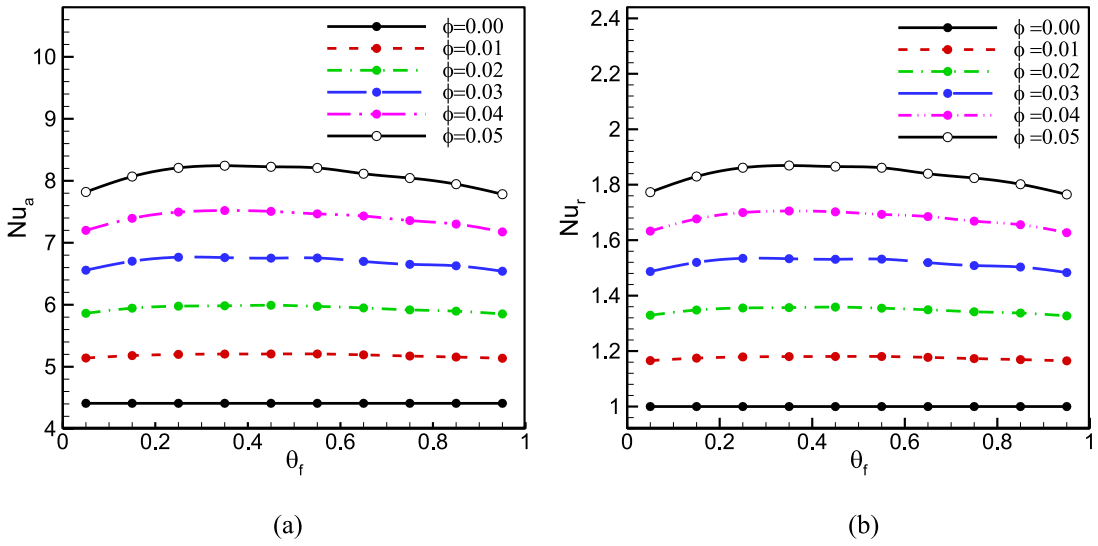

Fig. 8. Dependency of the Nu_a (a), and Nu_r (b) on the fusion temperature for different values of volume fraction and $Ste = 0.2$, $E_c = 0.75$, $\gamma = \pi/4$.

the variation of *Ste* seems to have little to no effect on Nu_a. The effect of θ_f on the variation of Nu_a is therefore similar to what was discussed in Fig. 8, i.e. an optimal heat transfer is obtained when θ_f diverges from the hot and cold walls temperatures. A maximum value of Nu_a is obtained for $Ste = 0.2$ and for $\theta_f = 0.3$.

Fig. 11 illustrates the effect of γ on the variation of Nu_a as a function of ϕ. The first observation is that Nu_a increases with ϕ and is maximum for $\phi = 0.05$, confirming the results discussed in Figs. 8 and 9. In addition, it can be seen that Nu_a rises with the decrease of γ and is maximum for $\gamma = -\pi/2$. This indicates that moving the inner cylinder

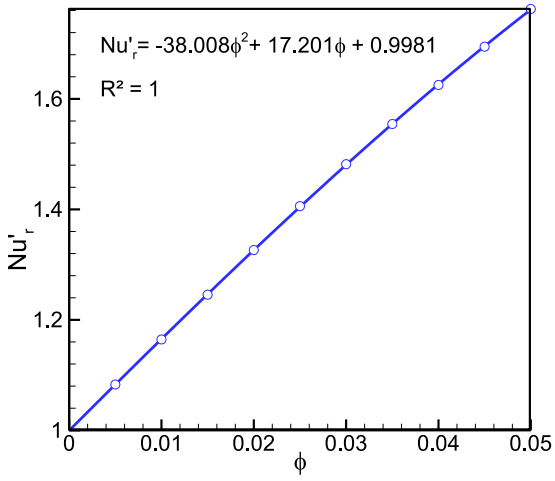

Fig. 9. Dependency of the Nu_r' on the volume fraction and $E_c = 0.75$, $\gamma = \pi/4$, $\theta_f = 0.05$.

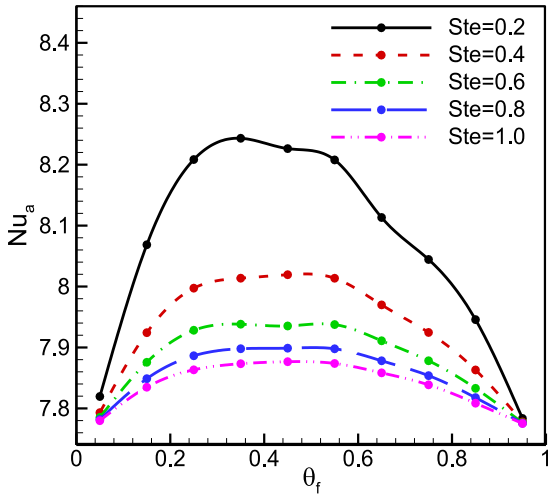

Fig. 10. Dependency of the average Nusselt number on the fusion temperature for different values of Stefan number and $\phi = 0.05$, $E_c = 0.75$, $\gamma = \pi/4$.

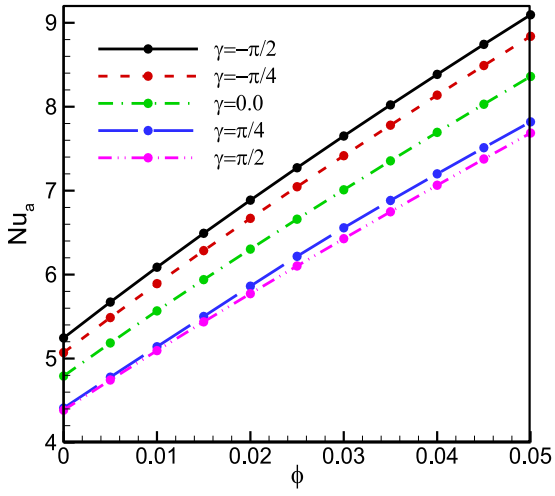

Fig. 11. Dependency of the average Nusselt number on the volume fractions at difference values of γ and $Ste = 0.2$, $\theta_f = 0.05$, and $E_c = 0.75$.

towards the bottom improves the heat transfer rate in the annulus. When the inner cylinder near the top, the upward motion of the hot fluid due is slowed down. Consequently, convective flow and heat

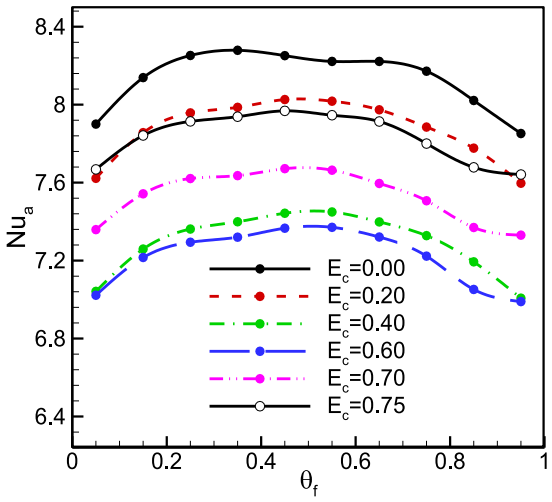

Fig. 12. Dependency of the average Nusselt number on the θ_f at difference values of eccentricity and $Ste = 0.3$, $\gamma = \pi/2$, and $\phi = 0.05$.

transfer are hindered and Nu_a is decreased.

Fig. 12 shows the variation of Nu_a for a range of fusion temperature values of θ_f and different values of E_c. The eccentricity angle is fixed at $\gamma = \pi/2$. It is shown that Nu_a increases with the decrease of E_c and reaches its maximum when the two cylinders are concentric, i.e. for $E_c = 0$. This is due to the fact that for $\gamma = \pi/2$, increasing E_c moves the inner cylinder to the top and consequently inhibits heat transfer as previously discussed. One would expect that for $\gamma = -\pi/2$, increasing E_c enhances heat transfer as the inner cylinder location would be moved downwards in that case.

The variation of Nu_r'' for a range of volume fraction of nanoparticles (ϕ) and various values of *Ste* is shown in Fig. 13. It is clear that when Nu_r'' is reduced when ϕ increases. This trend of variation is most obvious for $Ste = 0.2$. Nu_r'' represents the effect of the PCM phase change heat transfer by comparing a case of NEPCM suspension without phase change to the actual case. The result of Fig. 13 thus indicates that a suspension without phase change would have relatively less effect on heat transfer compared to one with phase change and that this disparity is most obvious for low *Ste*. This points out to the effect of the latent heat of the PCM phase change, as latent heat is increased for lower *Ste*.

5. Conclusion

The phase change heat transfer of nano-encapsulated phase change

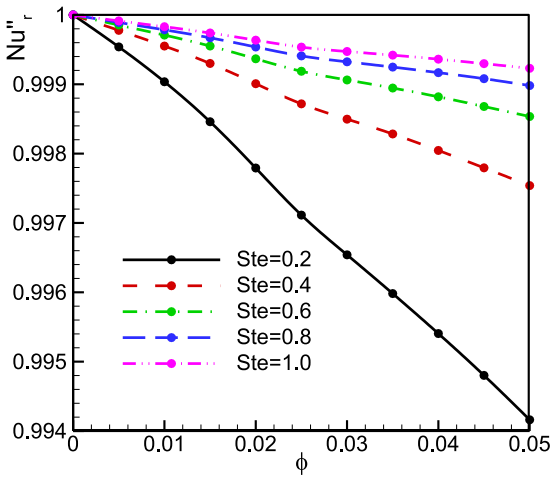

Fig. 13. Dependency of Nu_r'' on the volume fraction at difference values of Stefan number and $E_c = 0.75$, $\gamma = \pi/5$, and $\theta_f = 0.05$.

materials in an annulus was investigated for the different eccentric position of inner hot annuli. The non-dimensional form of the governing equations was solved using the FEM. The mesh independence-check and validations were performed. The effect of various parameters such as fusion temperature of PCM core of nanoparticles, latent heat capacity of nanoparticles (*Ste* number), and volume fraction of nanoparticles on the phase change heat transfer in the annulus cavity was addressed. The main outcomes of the current numerical investigation can be summed up as follows:

- Increasing the volume fraction of the NEPCM particles tends to enhance heat transfer in the annulus. 5% of NEPCM particles is the optimal volume fraction for heat transfer enhancement and for the assumption of a dilute suspension to be valid.
- A better heat transfer is achieved when the value of Stefan number *Ste* is decreased. The decrease of Stefan number can be seen as the raise of the latent heat of the PCM cores, which increases the contribution of the NEPCM particles to the overall heat transfer.
- Using NEPCM with fusion temperature θ_f close to the hot or the cold cylinder temperatures limits the area of phase change in the annulus and the heat transfer enhancement is hindered, due to the NEPCM particles, compared to particles with θ_f far from the cylinders' temperatures.
- Varying the eccentricity E_c and the eccentricity angle γ affects the heat transfer in the annulus depending on the location of the inner cylinder. Moving the inner cylinder upwards slows down the convective flow and inhibits heat transfer, while, conversely, shifting it upwards enhances the heat transfer in the annulus.

In the present study, the passive thermal behavior of a suspension of NEPCM particles in a shell and tube system is investigated. The results of the present work are limited to a dilute suspension of NEPCM particles due to the limitation of experimental data and models. However, a slurry of NEPCMs with much higher volume fraction of NEPCM particles is practical for energy storage systems. The increase of the volume fraction of NEPCM particles elevated the viscosity of the slurry and also leads to non-Newtonian effects. Although the increase of viscosity tends to suppress the natural convection flow, the increase of the latent heat of the slurry can be a decisive factor on improving the thermal response of the system. Hence, the experimental study of thermal behavior and energy storage of a slurry of NEPCMs containing a high volume fraction of NEPCM particles can be subject to future studies. Experimental data regarding the rheological behavior and thermal conductivity of a slurry of NEPCMs are essential for conducting future theoretical studies.

CRediT authorship contribution statement

S.A.M. Mehryan: Conceptualization, Methodology, Software, Validation, Data curation. **Mohammad Ghalambaz:** Conceptualization, Methodology, Validation, Data curation, Writing - original draft, Supervision, Project administration, Writing - review & editing. **Leila Sasani Gargari:** Visualization, Investigation. **Ahmad Hajjar:** Conceptualization, Methodology, Formal analysis, Investigation, Writing - review & editing. **Mikhail Sheremet:** Conceptualization, Writing - review & editing.

Declaration of Competing Interest

The authors declare that they have no known competing financial interests or personal relationships that could have appeared to influence the work reported in this paper.

Supplementary materials

Supplementary material associated with this article can be found, in the online version, at doi:10.1016/j.est.2020.101236.

Appendix A

FEM uses the interpolate (or shape) functions $\{\gamma_k\}_{k=1}^{N}$ to expand the governing variables as follows:

$$U \approx \sum_{m=1}^{N} U_m\gamma_m(X,\ Y),\ V \approx \sum_{m=1}^{N} V_m\gamma_m(X,\ Y),\ P \approx \sum_{m=1}^{N} P_m\gamma_m(X,\ Y),$$
$$\theta \approx \sum_{m=1}^{N} \theta_m\gamma_m(X,\ Y),\ \Psi \approx \sum_{m=1}^{N} \Psi_m\gamma_m(X,\ Y) \tag{A1}$$

By employing the Galerkin approach, the residual equations for the above variables at each element can be written as:

$$R_i^1 \approx \left(\frac{\rho_b}{\rho_f}\right)\sum_{m=1}^{N} U_m \int\left[\left(\sum_{m=1}^{N} U_m\gamma_m\right)\frac{\partial\gamma_m}{\partial X} + \left(\sum_{k=1}^{N} V_m\gamma_m\right)\frac{\partial\gamma_m}{\partial Y}\right]\gamma_i dXdY$$
$$- \sum_{m=1}^{N}\int\left(\sum_{m=1}^{N} P_m\gamma_m\right)\frac{\partial\gamma_m}{\partial X}\gamma_i dXdY + Pr\left(\frac{\mu_b}{\mu_f}\right)\sum_{m=1}^{N} U_m\int\left[\frac{\partial\gamma_m}{\partial Y}\frac{\partial\gamma_i}{\partial Y}\right]dXdY$$
$$Pr\left(\frac{\mu_b}{\mu_f}\right)\sum_{m=1}^{N} U_m\int\left[\frac{\partial\gamma_m}{\partial X}\frac{\partial\gamma_i}{\partial X}\right]dXdY \tag{A2}$$

$$R_i^2 \approx \left(\frac{\rho_b}{\rho_f}\right)\sum_{m=1}^{N} V_m \int\left[\left(\sum_{m=1}^{N} U_m\gamma_m\right)\frac{\partial\gamma_m}{\partial X} + \left(\sum_{k=1}^{N} V_m\gamma_m\right)\frac{\partial\gamma_m}{\partial Y}\right]\gamma_i dXdY$$
$$- \sum_{m=1}^{N}\int\left(\sum_{m=1}^{N} P_m\gamma_m\right)\frac{\partial\gamma_i}{\partial Y}dXdY + Pr\left(\frac{\mu_b}{\mu_f}\right)\sum_{m=1}^{N} V_m\int\left[\frac{\partial\gamma_m}{\partial X}\frac{\partial\gamma_i}{\partial X}\right]dXdY$$
$$+ Pr\left(\frac{\mu_b}{\mu_f}\right)\sum_{m=1}^{N} V_m\int\left[\frac{\partial\gamma_m}{\partial Y}\frac{\partial\gamma_i}{\partial Y}\right]dXdY + Ra\cdot Pr\left(\frac{\rho_b}{\rho_f}\right)\left(\frac{\beta_b}{\beta_f}\right)\int\left(\sum_{m=1}^{N}\theta_m\gamma_m\right)\gamma_i dXdY \tag{A3}$$

$$R_i^3 \approx \sum_{m=1}^{N} U_m\int\frac{\partial\gamma_m}{\partial X}\gamma_i dXdY + \sum_{m=1}^{N} V_m\int\frac{\partial\gamma_m}{\partial Y}\gamma_i dXdY \tag{A4}$$

$$R_i^4 \approx Cr\sum_{m=1}^{N}\theta_m \int\left[\left(\sum_{m=1}^{N} U_m\gamma_m\right)\frac{\partial\gamma_m}{\partial X} + \left(\sum_{m=1}^{N} V_m\gamma_m\right)\frac{\partial\gamma_m}{\partial Y}\right]\gamma_m dXdY$$
$$+ \left(\frac{k_b}{k_f}\right)\sum_{m=1}^{N}\theta_m\int\left[\frac{\partial\gamma_m}{\partial X}\frac{\partial\gamma_i}{\partial X} + \frac{\partial\gamma_m}{\partial Y}\frac{\partial\gamma_i}{\partial Y}\right]dXdY \tag{A5}$$

$$R_i^5 \approx \sum_{m=1}^{N} \Psi_m \int \left[\frac{\partial \gamma_m}{\partial X}\frac{\partial \gamma_i}{\partial X} + \frac{\partial \gamma_m}{\partial Y}\frac{\partial \gamma_i}{\partial Y} \right] dXdY$$
$$+ \int \left[\left(\sum_{m=1}^{N} U_m \gamma_m\right)\frac{\partial \gamma_m}{\partial Y} - \left(\sum_{k=1}^{N} V_m \gamma_m\right)\frac{\partial \gamma_m}{\partial X} \right] \gamma_i dXdY \quad \text{(A6)}$$

Eqs. (A2)–(A6) represents the residual equations for the finite element method. The equations are obtained by writing the governing equations into the weak form and then substituting the basis functions. For each element there is a set of residual equations produced from the interaction of Eqs. (A2)–(A6). It should be noted that although the integrations are performed over the entire domain, the equations are non-zero only at the element.

References

[1] B. Kahouli, Does static and dynamic relationship between economic growth and energy consumption exist in OECD countries? Energy Reports 5 (2019) 104–116.
[2] R. Waheed, S. Sarwar, C. Wei, The survey of economic growth, energy consumption and carbon emission, Energy Reports 5 (2019) 1103–1115.
[3] J.M. Mahdi, S. Lohrasbi, E.C. Nsofor, Hybrid heat transfer enhancement for latent-heat thermal energy storage systems: a review, Int. J. Heat Mass Transf. 137 (2019) 630–649.
[4] L.N. Narasimhan, Assessment of latent heat thermal storage systems operating with multiple phase change materials, J. Energy Storage 23 (2019) 442–455.
[5] P.K.S. Rathore, S.K. Shukla, Potential of macroencapsulated pcm for thermal energy storage in buildings: a comprehensive review, Constr. Build. Mater. 225 (2019) 723–744.
[6] M. Fadl, P.C. Eames, An experimental investigation of the heat transfer and energy storage characteristics of a compact latent heat thermal energy storage system for domestic hot water applications, Energy (2019) 116083.
[7] Y. Wang, K. Yu, X. Ling, Experimental and modeling study on thermal performance of hydrated salt latent heat thermal energy storage system, Energy Convers. Manage. 198 (2019) 111796.
[8] V. Vigneswaran, G. Kumaresan, B. Dinakar, K.K. Kamal, R. Velraj, Augmenting the productivity of solar still using multiple PCMs as heat energy storage, J. Energy Storage 26 (2019) 101019.
[9] B. Buonomo, H. Celik, D. Ercole, O. Manca, M. Mobedi, Numerical study on latent thermal energy storage systems with aluminum foam in local thermal equilibrium, Appl. Therm. Eng. (2019) 113980.
[10] V. Joshi, M.K. Rathod, Thermal transport augmentation in latent heat thermal energy storage system by partially filled metal foam: a novel configuration, J. Energy Storage 22 (2019) 270–282.
[11] M. Rahimi, S.S. Ardahaie, M. Hosseini, M. Gorzin, Energy and exergy analysis of an experimentally examined latent heat thermal energy storage system, Renew. Energy (2019).
[12] M. Zeneli, I. Malgarinos, A. Nikolopoulos, N. Nikolopoulos, P. Grammelis, S. Karellas, E. Kakaras, Numerical simulation of a silicon-based latent heat thermal energy storage system operating at ultra-high temperatures, Appl. Energy 242 (2019) 837–853.
[13] K.Y. Leong, M.R.A. Rahman, B.A. Gurunathan, Nano-enhanced phase change materials: a review of thermo-physical properties, applications and challenges, J. Energy Storage 21 (2019) 18–31.
[14] M. Gorzin, M.J. Hosseini, M. Rahimi, R. Bahrampoury, Nano-enhancement of phase change material in a shell and multi-PCM-tube heat exchanger, J. Energy Storage 22 (2019) 88–97.
[15] A.M. Abdulateef, J. Abdulateef, A.A. Al-Abidi, K. Sopian, S. Mat, M.S. Mahdi, A combination of fins-nanoparticle for enhancing the discharging of phase-change material used for liquid desiccant air conditioning unite, J. Energy Storage 24 (2019) 100784.
[16] N.S. Bondareva, B. Buonomo, O. Manca, M.A. Sheremet, Heat transfer performance of the finned nano-enhanced phase change material system under the inclination influence, Int. J. Heat Mass Transf. 135 (2019) 1063–1072.
[17] F. Rodríguez-Cumplido, E. Pabón-Gelves, F. Chejne-Jana, Recent developments in the synthesis of microencapsulated and nanoencapsulated phase change materials, J. Energy Storage 24 (2019) 100821.
[18] M. Ghalambaz, A.J. Chamkha, D. Wen, Natural convective flow and heat transfer of Nano-Encapsulated Phase Change Materials (NEPCMs) in a cavity, Int. J. Heat Mass Transf. 138 (2019) 738–749.
[19] A. Hajjar, S. Mehryan, M. Ghalambaz, Time periodic natural convection heat transfer in a nano-encapsulated phase-change suspension, Int. J. Mech. Sci. (2019) 105243.
[20] X. Cao, Y. Yuan, B. Xiang, F. Haghighat, Effect of natural convection on melting performance of eccentric horizontal shell and tube latent heat storage unit, Sustain. Cities Soc. 38 (2018) 571–581.
[21] R. Senthil, Effect of position of heat transfer fluid tube on the melting of phase change material in cylindrical thermal energy storage, energy sources, part A: recovery, Utilization Environ. Eff. (2019) 1–11.
[22] M. Kadivar, M. Moghimi, P. Sapin, C. Markides, Annulus eccentricity optimisation of a phase-change material (PCM) horizontal double-pipe thermal energy store, J Energy Storage 26 (2019) 101030.
[23] L. Kalapala, J.K. Devanuri, Influence of operational and design parameters on the performance of a PCM based heat exchanger for thermal energy storage–A review, J. Energy Storage 20 (2018) 497–519.
[24] M.D.P.R. Teles, K.A. Ismail, A. Arabkoohsar, A new version of a low concentration evacuated tube solar collector: optical and thermal investigation, Sol. Energy 180 (2019) 324–339.
[25] S. Barlak, O.N. Sara, A. Karaipekli, S. Yapıcı, Thermal conductivity and viscosity of nanofluids having nanoencapsulated phase change material, Nanoscale Microscale Thermophys. Eng. 20 (2) (2016) 85–96.
[26] L. Chai, R. Shaukat, L. Wang, H.S. Wang, A review on heat transfer and hydrodynamic characteristics of nano/microencapsulated phase change slurry (N/MPCS) in mini/microchannel heat sinks, Appl. Therm. Eng. 135 (2018) 334–349.
[27] B. Chen, X. Wang, R. Zeng, Y. Zhang, X. Wang, J. Niu, Y. Li, H. Di, An experimental study of convective heat transfer with microencapsulated phase change material suspension: laminar flow in a circular tube under constant heat flux, Exp. Therm. Fluid Sci. 32 (8) (2008) 1638–1646.
[28] K. Khanafer, K. Vafai, A critical synthesis of thermophysical characteristics of nanofluids, Int. J. Heat Mass Transf. 54 (19–20) (2011) 4410–4428.
[29] H.R. Seyf, Z. Zhou, H. Ma, Y. Zhang, Three dimensional numerical study of heat-transfer enhancement by nano-encapsulated phase change material slurry in microtube heat sinks with tangential impingement, Int. J. Heat Mass Transf. 56 (1–2) (2013) 561–573.
[30] A. Zaraki, M. Ghalambaz, A.J. Chamkha, M. Ghalambaz, D. De Rossi, Theoretical analysis of natural convection boundary layer heat and mass transfer of nanofluids: effects of size, shape and type of nanoparticles, type of base fluid and working temperature, Adv. Powder Technol. 26 (3) (2015) 935–946.
[31] A. Chamkha, A. Doostanidezfuli, E. Izadpanahi, M. Ghalambaz, Phase-change heat transfer of single/hybrid nanoparticles-enhanced phase-change materials over a heated horizontal cylinder confined in a square cavity, Adv. Powder Technol. 28 (2) (2017) 385–397.
[32] O. Schenk, K. Gärtner, Solving unsymmetric sparse systems of linear equations with PARDISO, Future Gener. Comput. Syst. 20 (3) (2004) 475–487.
[33] P. Wriggers, Nonlinear Finite Element Methods, Springer Science & Business Media, 2008.
[34] F. Verbosio, A. De Coninck, D. Kourounis, O. Schenk, Enhancing the scalability of selected inversion factorization algorithms in genomic prediction, J. Comput. Sci. 22 (2017) 99–108.
[35] O. Schenk, K. Gärtner, Pardiso, Encyclopedia of Parallel Computing, (2011), pp. 1458–1464.
[36] M.H. Matin, I. Pop, Natural convection flow and heat transfer in an eccentric annulus filled by copper nanofluid, Int. J. Heat Mass Transf. 61 (2013) 353–364.
[37] O. Turan, A. Sachdeva, N. Chakraborty, R.J. Poole, Laminar natural convection of power-law fluids in a square enclosure with differentially heated side walls subjected to constant temperatures, J. Nonnewton. Fluid Mech. 166 (17) (2011) 1049–1063.
[38] T. Kuehn, R. Goldstein, An experimental and theoretical study of natural convection in the annulus between horizontal concentric cylinders, J. Fluid Mech. 74 (4) (1976) 695–719.